Super-resolution video microscopy of live cells by structured illumination

Peter Kner[1,2,7,8], Bryant B Chhun[1,8], Eric R Griffis[3,4], Lukman Winoto[5] & Mats G L Gustafsson[5,6]

Structured-illumination microscopy can double the resolution of the widefield fluorescence microscope but has previously been too slow for dynamic live imaging. Here we demonstrate a high-speed structured-illumination microscope that is capable of 100-nm resolution at frame rates up to 11 Hz for several hundred time points. We demonstrate the microscope by video imaging of tubulin and kinesin dynamics in living *Drosophila melanogaster* S2 cells in the total internal reflection mode.

The fluorescence microscope is an essential tool in many fields of biology but, in its classic form, is incapable of spatial resolution better than about 200 nm because of diffraction. Several recent methods can go well beyond this limit[1–6], within the constraints of each technique. Localization-based methods such as photo-activated localization microscopy (PALM)[4], stochastic optical reconstruction microscopy (STORM)[5] and fluorescence photo-activation localization microscopy (FPALM)[6] can achieve extreme resolution by precisely localizing individual photoactivatable fluorophores but require very large numbers of raw images (hundreds to tens of thousands) and are therefore limited in speed. A recent form of PALM decreases the acquisition time for a single frame from hours to around 25–60 s and has recorded movies of ~20 frames; the downside is that only a subset of molecules are located per frame, which limits[7] the effective resolution to ~60 nm. Stimulated emission depletion microscopy (STED) has obtained resolution below 30 nm by de-exciting the edges of the illuminated scan spot through stimulated emission[1]. STED has achieved an impressive frame rate of 28 frames per second at 62-nm resolution[8], though with low photon counts and over a relatively small field of view of 2.5 × 1.8 μm. Enlarging the field of view would directly decrease the frame rate, because STED is a point-scanning method. There is still a need for a technique that can combine spatial super-resolution with multihertz frame rates over large fields of view.

In structured-illumination microscopy (SIM), resolution is improved by moving high-resolution information into the normal resolution passband through spatial frequency mixing with an illumination pattern[2]. It can improve resolution by a factor of two in its linear form, and by a larger factor if nonlinearity can be exploited[3]. Linear SIM achieves a resolution of about 100 nm, not quite as high as the above methods, but has potential for (i) much higher frame rates than PALM because it requires fewer raw data images and (ii) much larger fields of view than high-speed STED at a given frame rate because it acquires pixels in parallel by wide-field imaging rather than sequentially by point scanning.

In microscopy in general, the highest frame rates are possible when the region of interest is thin enough that only a single plane, rather than a focal series, needs to be acquired at each time point. Indeed, to our knowledge all super-resolution time series published so far have been two-dimensional (2D)[7,8]. Total internal reflection fluorescence (TIRF) microscopy provides an extremely thin emitting region, which can be treated as 2D for SIM purposes. SIM has already been used in TIRF microscopy[9–13] but not for time-series imaging of live samples. Here we demonstrate live TIRF SIM at 100-nm resolution, with 3.7–11 Hz frame rates over fields of view of 32 × 32 to 8 × 8 μm.

Our implementation of 2D SIM uses nine raw images, acquired with different illumination patterns, to construct one high-resolution output image: a periodic pattern of parallel lines is shifted through three phases for each of three orientation angles[2]. (We refer to such a set of nine raw images, yielding one SIM reconstruction, as a "SIM frame" or "time point".) Our original SIM had produced the pattern with a transmission phase grating that was translated by a piezoelectric actuator and rotated by a mechanical stage[2]. The mechanical movement of the grating was slow and limited the acquisition speed to several seconds per SIM frame. For this work we decreased the pattern-switching time by three orders of magnitude by using a ferroelectric liquid crystal on silicon spatial light modulator (SLM) to produce the patterns (**Supplementary Figs. 1–4** online). To switch patterns we simply wrote new digital image data to the SLM (**Supplementary Fig. 2**), which takes only 0.6 ms; the response time of the ferroelectric liquid crystal is even faster and does not limit the switching speed. The SLM consists of 1,024 × 768 pixels, enough to illuminate the full field of view of our camera.

The pattern can be thought of as formed by interference of two collimated beams, created by diffraction from the SLM. For maximum signal the interference contrast must be maximized, which requires the two beams to be linearly polarized parallel to the pattern lines; the polarization must thus be co-rotated with the pattern orientation. We implemented polarization rotation with two custom ferroelectric liquid crystal switchable retarders (Displaytech; **Supplementary Fig. 3**). Their switching time of

[1]Department of Biochemistry and Biophysics, [2]Keck Advanced Microscopy Laboratory, [3]Department of Cellular and Molecular Pharmacology, [4]Howard Hughes Medical Institute and [5]Department of Physiology and Program in Bioengineering, University of California San Francisco, San Francisco California, USA. [6]Howard Hughes Medical Institute, Janelia Farm Research Campus, Ashburn, Virginia, USA. [7]Present address: Faculty of Engineering, University of Georgia, Athens, Georgia, USA. [8]These authors contributed equally to this work. Correspondence should be addressed to M.G.L.G. (gustafssonm@janelia.hhmi.org).

RECEIVED 21 NOVEMBER 2008; ACCEPTED 21 MARCH 2009; PUBLISHED ONLINE 26 APRIL 2009; DOI:10.1038/NMETH.1324

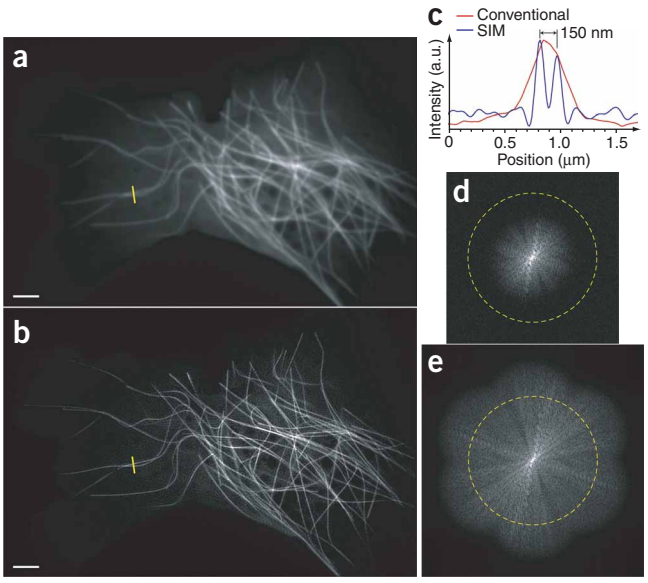

Figure 1 | Comparison of TIRF-SIM and conventional TIRF microscopy. (**a**,**b**) Conventional TIRF microscopy (**a**) and TIRF-SIM (**b**) images of the microtubule cytoskeleton in a single S2 cell. Scale bars, 2 μm. (**c**) Normalized intensity profiles along the yellow lines in **a** and **b**. Two microtubules separated by ~150 nm are well resolved in the SIM reconstruction, but not by conventional microscopy. (**d**,**e**) Fourier transforms of the images in **a** (**d**) and **b** (**e**). The classical diffraction limit of the objective lens is indicated by a dashed circle of radius 5.96 μm^{-1}. Sample information is visible as a bright 'starburst' in the low-spatial-frequency central region of **d**. That it does not reach the diffraction limit indicates that the effective resolution is lower than theory predicts, as is true for most high-numerical aperture (NA) objectives. The same sample information features can be recognized in **e**, where they continue out to higher spatial frequencies, well beyond the diffraction limit.

<100 μs was concurrent with SLM pattern switching and did not add to the acquisition time. The time required for one raw data image was thus dominated by the readout time of the camera or by the exposure time if that was longer. In our microscope we used a 512 × 512 pixel frame-transfer electron-multiplying charge-coupled device (EMCCD) camera with a maximum full-frame rate of 35 Hz; the corresponding maximum SIM frame rate was one-ninth of that or about 3.9 Hz. When the full field of view was not needed, the SIM frame rate could be increased by reading out a subfield (for example, the maximum rate at 128 × 128 pixels would be 14.7 Hz). The SIM frame rate could be increased more drastically by using a camera with fewer pixels and correspondingly higher raw frame rate. The SIM reconstructions have twice as many pixels in each dimension as the raw data. Our current full field of view is 32 × 32 μm, but could be increased to 43 × 43 μm for the same camera without undersampling.

As a first demonstration, we imaged α-tubulin fused to enhanced GFP (EGFP) in living *Drosophila* S2 cells, at illumination intensities of approximately 5–10 W cm^{-2}. To bring more microtubules into the region illuminated by TIRF, we used an established protocol that gently flattens the cells by mechanical pressure against a pad of agarose gel (Online Methods). SIM produces a striking resolution improvement over conventional TIRF microscopy, as can be seen both in real space (**Fig. 1a–c** and **Supplementary Video 1** online) and in frequency space (**Fig. 1d**,**e** and **Supplementary Video 2** online). The full width at half maximum (FWHM) of isolated microtubules was 112 ± 12 nm in the SIM reconstructions, compared to 275 ± 21 nm in the conventional images (based on 158 measurements on 8 datasets). On test samples with 100 nm fluorescent microspheres, we measured an average FWHM of 104 nm (data not shown).

Time series with hundreds of time points can be produced using this method (see **Supplementary Videos 1**, **3** and **4** online for examples with 120, 200 and 480 time points, respectively). One of these datasets (**Supplementary Video 3**) depicts microtubule dynamics in a tripolar mitotic spindle (multiple centrosomes are common in S2 cells). In the 480-SIM-frame dataset, microtubule segments that were present in all frames photobleached by approximately 50%; segments that polymerized during the experiment were correspondingly less affected by bleaching.

To evaluate live SIM as a tool for studying microtubule polymerization and depolymerization dynamics, we imaged the area near a centrosome of a mitotic S2 cell (**Fig. 2** and **Supplementary Video 5** online). A useful way to visualize these processes is with kymographs, using the random variation in fluorescence labeling density along each microtubule (speckling) to track microtubule position and thereby distinguish overall movement of the microtubule from growth or shrinkage at the end. Because of its higher resolution, SIM can be used to visualize speckling with enhanced clarity (**Fig. 2c** and **Supplementary Video 6** online) and permits increased labeling densities that allow more precise localization of the microtubule end. Even when the signal-to-noise ratio at each time point was low, the time series nature of the data allowed true labeling density variations to be distinguished from noise in that they persisted over time and moved with the microtubules (**Supplementary Fig. 5** online). We often observed sudden transitions between states of steady polymerization or depolymerization, paused states of constant length and states of slower or less stable evolution (**Fig. 2c**). With conventional microscopy, the speckling was much less sharp and harder to distinguish from background features such as the coarse horizontal stripes caused by exclusion of free monomeric EGFP–α-tubulin by organelles. The rates of steady polymerization and depolymerization that we observed in such kymographs, 87 ± 26 nm s^{-1} and 267 ± 56 nm s^{-1} respectively (each averaged over 22 measurements), were comparable to values reported in the literature[14] for S2 cells (107 ± 55 nm s^{-1} and 233 ± 75 nm s^{-1}).

The ability of live SIM to resolve single microtubules in the spindle and follow their individual movements and polymerization activity makes new experiments possible. For example, it has been suggested that microtubules can nucleate in the spindle through an augmin-mediated pathway[15]. Live SIM should allow this process to be visualized directly. As a second example, microtubules in mitotic (or meiotic) spindles can exhibit 'poleward flux' toward the centrosome, a phenomenon that has typically been studied collectively, for example, by spot photobleaching of entire kinetochore fibers that contain multiple microtubules[16] or by microinjection of dye-labeled tubulin at such low densities that different speckles likely belong to different microtubules[17]. With the higher resolution of SIM, poleward movement of spindle microtubules can be visualized and quantified in single microtubules (**Supplementary Fig. 6** online) and correlated with observed polymerization activity at the microtubule end.

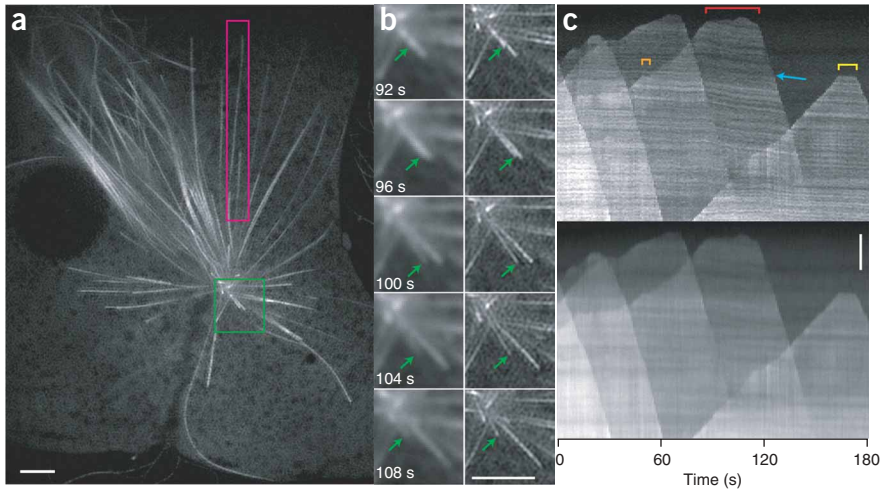

Figure 2 | Time series live TIRF-SIM of EGFP–α-tubulin in an S2 cell. (**a**) Part of the field of view of one SIM frame (number 95) from a 180-frame sequence. Each SIM frame was acquired in 270 ms (that is, a raw data exposure time of 30 ms), using the full 512 × 512 pixel field of view of the camera. SIM frames were deliberately spaced at 1-s intervals. (**b**) Conventional TIRF microscopy (left) and TIRF-SIM (right) images of the boxed region (green) in **a** at the indicated times. The contrast of the conventional images has been increased for clarity. Arrows indicate the end of one particular microtubule, which can be seen elongating until approximately the 100 s time point and then rapidly shrinking; these changes are easier to follow in the SIM reconstruction. (**c**) Maximum-intensity kymographs, using TIRF-SIM (top) and conventional TIRF (bottom), of the rectangular region in **a** (magenta). Five separate microtubules are seen expanding and contracting through the area. One microtubule in particular is retracting noticeably, causing tilted lines in the kymograph (arrow). Sharp transitions separate periods of steady polymerization or depolymerization from periods of constant length (examples indicated by yellow and orange brackets), or of slower and less stable growth or shrinkage (red bracket). Some constant-length periods are followed by resumed polymerization (orange bracket), others by rapid depolymerization (yellow bracket). Scale bars, 2 μm.

As a challenging test case with very rapidly moving structures, we imaged kinesin-73–EGFP in S2 cells. Kinesin travels actively along microtubules at a typical speed[18] of about 780 nm s^{-1}, corresponding to one 100-nm SIM resolution distance in about 130 ms; to avoid artifacts, the time to acquire one SIM frame should be comparable or shorter. A time series with 144 ms SIM frame time (16-ms exposures), acquired with a 256 × 256 pixel field, produced a clear reconstruction in which individual kinesin-cargo complexes could be followed along microtubule tracks (**Fig. 3** and **Supplementary Videos 7** and **8** online). The nominal illumination intensity for this data set was ~26 W cm^{-2}, and over 120 time points the average image intensity decreased by about a factor of 3 due to photobleaching. Those kinesin spots that appeared to move progressively along tracks did so at speeds of 0.4–0.9 μm s^{-1}, in reasonable agreement with expectations for kinesin. Still smaller fields of view allowed even higher SIM frame rates; over a 128 × 128 pixel field (corresponding to 256 × 256 pixels after reconstruction) we imaged kinesin dynamics at a SIM frame rate of 11.1 Hz (**Supplementary Video 9** online). The signal-to-noise ratio decreased at high imaging speed, but the resolution was not severely affected: the average FWHM apparent size of persistent kinesin complexes in the 11-Hz dataset was 112 ± 13 nm ($n = 30$), identical to the average FWHM observed in the slower tubulin data.

A critical requirement in live SIM is that the image sequence for a given time point should be acquired in a time short enough that no fine sample features move by more than about one resolution

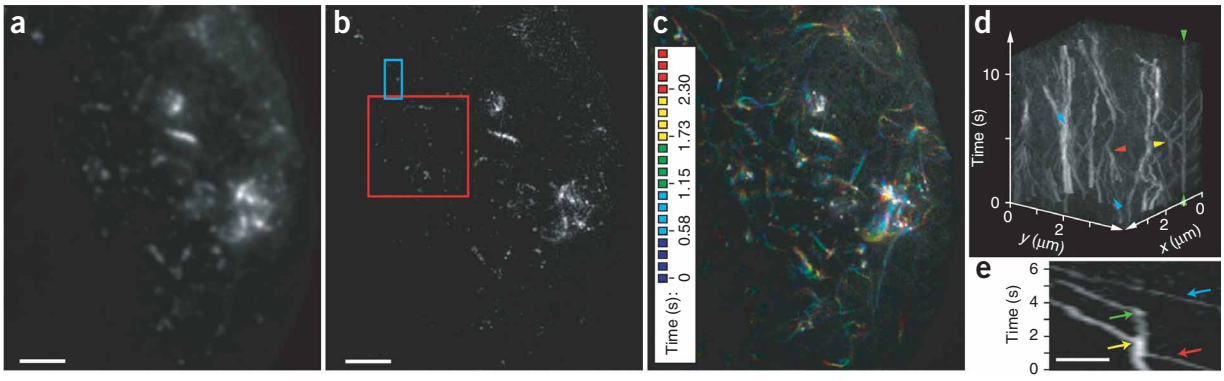

Figure 3 | Time-series live TIRF-SIM of kinesin-73–EGFP in an S2 cell. (**a**,**b**) Conventional TIRF microscopy (**a**) and TIRF-SIM (**b**) images of the first of 120 time points. Each SIM frame was acquired in 144 ms (that is, a raw data exposure time of 16 ms), using a 256 × 256 pixel field of view. (**c**) Projection of the first 20 TIRF-SIM frames, color-coded for time. Moving and stationary kinesin-cargo complexes can be seen as multicolored curves and white spots respectively. (**d**) A 3D maximum-intensity kymograph of the boxed area in **b** (red), covering the first 80 SIM frames. Kinesin spots exhibited various behaviors, including clustering together (red arrowhead), splitting or separating (yellow arrowhead), remaining stationary (vertical line between the green arrowheads), and traveling at a constant velocity (inclined straight line between the blue arrowheads). (**e**) Kymograph produced by maximum-intensity projecting the area marked by the blue rectangle in **b** onto the *y* axis for each of the first 46 time points. A traveling kinesin complex (red arrow) joined a nearly stationary kinesin complex (bottom center) and halted. After a 0.6 s pause, one kinesin complex traveled onward (yellow arrow), while the other remained stationary for another 1.8 s, at which time it also resumed forward travel (green arrow). A third kinesin complex that traveled past later, possibly along the same microtubule, did not pause (blue arrow). Scale bars, 2 μm (**a**–**c**) and 0.5 μm (**e**).

length, to avoid reconstruction artifacts (**Supplementary Fig. 7** online). For this reason, high acquisition speed is beneficial even in situations when observations are to be sparsely spaced in time (which may be desired for studying a long-term process without observing so many times as to cause excessive photobleaching): each SIM sequence can be acquired rapidly enough to prevent artifacts, and successive sequences can be spaced out by appropriate delay times.

Our approach to live SIM could be extended in several ways. For example, multiple emission colors could be imaged simultaneously by adding cameras or split-view devices. The current design is limited to a single excitation wavelength (because the beam spacing, which must match the pupil diameter, is produced by diffraction and therefore proportional to the wavelength), but one excitation wavelength can be used to excite multiple fluorophores with different emission bands[19]. Drastically higher frame rates would be possible by using faster cameras, though typically at a cost of either field of view or sensitivity. For example, existing 128 × 128 pixel EMCCD cameras could allow TIRF-SIM at over 50 SIM frames per second over a ~13 × 13 μm area. It may be possible to achieve even higher spatial resolution through nonlinear SIM[3], but this requires a larger number of raw images per SIM frame and the use of photoswitchable dyes or fluorescence saturation methods, and puts greater demands on photostability. The hardware used here for 2D TIRF-SIM could also be used for three-dimensional (3D) SIM[20] with only minor modifications: slightly different SLM patterns and a different demagnification factor from the SLM to the sample (**Supplementary Note** online). The frame rate would be slower in 3D SIM than in 2D SIM owing to the larger number of raw images per SIM frame: at each time point 3D SIM would use a focal series of axial planes spaced about 150 nm apart and 15 instead of 9 raw images per axial plane[20]. Live 3D SIM would therefore become less tolerant of sample motion, in proportion to the sample thickness, but appears promising for relatively thin samples.

Although linear SIM does not produce quite as high resolution as STED or PALM, its frame rate and number of time points exceed those of live PALM by an order of magnitude, and the area rates (product of frame rate and field of view) exceed those published for live STED by a similar factor. Speckle microscopy, as in the experiment shown in **Figure 2c**, is not compatible with PALM as published, which images disjoint subsets of molecules, with statistically independent random variations, at different time points.

In summary, SLM-based SIM offers a combination of increased resolution, multihertz live imaging, long time series and large field of view that other super-resolution techniques do not provide, and does so without requiring special fluorophores or extreme light intensities.

METHODS

Methods and any associated references are available in the online version of the paper at http://www.nature.com/naturemethods/.

Note: Supplementary information is available on the Nature Methods website.

ACKNOWLEDGMENTS

We thank T. Huckaba for generating the kinesin-73-EGFP cell line; L. Shao, S. Haase and the late Melvin Jones for help with software; D. Agard and J. Sedat for their role in the development of structured-illumination microscopy; R. Vale (University of California, San Francisco) for his support of E.R.G, for the GFP-α-tubulin S2 cell line and for useful comments; and R. Oldenbourg for a useful discussion. This work was supported in part by the David and Lucile Packard Foundation, the Sandler Family Supporting Foundation, the Keck Advanced Microscopy Laboratory, the Howard Hughes Medical Institute and by the US National Science Foundation through the Center for Biophotonics, a National Science Foundation Science and Technology Center that is managed by the University of California, Davis, under Cooperative Agreement PHY 0120999.

AUTHOR CONTRIBUTIONS

P.K. designed and built the rapid control system and wrote the manuscript draft. B.B.C. acquired and processed the data. L.W., B.B.C. and P.K. built optical hardware. E.R.G. prepared the samples. M.G.L.G. made the conceptual design and wrote the simulation. B.B.C. and M.G.L.G. analyzed data. B.B.C., M.G.L.G. and E.R.G. edited the manuscript.

COMPETING INTERESTS STATEMENT

The authors declare competing financial interests: details accompany the full-text HTML version of the paper at http://www.nature.com/naturemethods/.

Published online at http://www.nature.com/naturemethods/
Reprints and permissions information is available online at http://npg.nature.com/reprintsandpermissions/

1. Willig, K.I., Rizzoli, S.O., Westphal, V., Jahn, R. & Hell, S.W. *Nature* **440**, 935–939 (2006).
2. Gustafsson, M.G.L. *J. Microsc.* **198**, 82–87 (2000).
3. Gustafsson, M.G.L. *Proc. Natl. Acad. Sci. USA* **102**, 13081–13086 (2005).
4. Betzig, E. *et al. Science* **313**, 1642–1645 (2006).
5. Rust, M.J., Bates, M. & Zhuang, X. *Nat. Methods* **3**, 793–796 (2006).
6. Hess, S.T., Girirajan, T.P. & Mason, M.D. *Biophys. J.* **91**, 4258–4272 (2006).
7. Shroff, H., Galbraith, C.G., Galbraith, J.A. & Betzig, E. *Nat. Methods* **5**, 417–423 (2008).
8. Westphal, V. *et al. Science* **320**, 246–249 (2008).
9. Chung, E., Kim, D., Cui, Y., Kim, Y.H. & So, P.T. *Biophys. J.* **93**, 1747–1757 (2007).
10. Gliko, O., Reddy, G.D., Anvari, B., Brownell, W.E. & Saggau, P. *J. Biomed. Opt.* **11**, 064013 (2006).
11. Gliko, O., Reddy, G.D., Brownell, W.E. & Saggau, P. *Proc. SPIE* **6861** 68610B–1 (2008).
12. Fiolka, R., Beck, M. & Stemmer, A. *Opt. Lett.* **33**, 1629–1631 (2008).
13. Beck, M., Aschwanden, M. & Stemmer, A. *J. Microsc.* **232**, 99–105 (2008).
14. Mennella, V. *et al. Nat. Cell Biol.* **7**, 235–245 (2005).
15. Goshima, G., Mayer, M., Zhang, N., Stuurman, N. & Vale, R.D. *J. Cell Biol.* **181**, 421–429 (2008).
16. Buster, D.W., Zhang, D. & Sharp, D.J. *Mol. Biol. Cell* **18**, 3094–3104 (2007).
17. Brust-Mascher, I., Sommi, P., Cheerambathur, D.K. & Scholey, J.M. *Mol. Biol. Cell* **20**, 1749–1762 (2009).
18. Cai, D., Verhey, K.J. & Meyhofer, E. *Biophys. J.* **92**, 4137–4144 (2007).
19. Kogure, T. *et al. Nat. Biotechnol.* **24**, 577–581 (2006).
20. Gustafsson, M.G.L. *et al. Biophys. J.* 107.120345 (2008).

ONLINE METHODS

Cell maintenance and preparation. *Drosophila* S2 cells stably expressing EGFP–α-tubulin under the control of the *Ac5* promoter were maintained as described[21]. The gene encoding full-length KHC-73 was cloned from pooled cDNA, ligated into pENTR-D-Topo (Invitrogen) and inserted into a Gateway vector under the control of the metallothionein promoter[22]. S2 cells stably transfected with this construct were selected, and protein expression was induced with 20 μm $CuSO_4$ 24 h before imaging.

To prepare cells for imaging, exponentially growing cells were resuspended in their conditioned medium to a concentration of 2×10^7 cells ml^{-1}, and 30 μl of this suspension was pipeted onto a cleaned 24 × 50 mm #1.5 coverslip and covered with a piece of 170-μm-thick 2% agarose gel, as described[23] except omitting the spacers. The agarose pad was covered with a 22 × 22 mm coverslip and sealed with valap. Samples were imaged through the 24 × 50 mm coverslip.

Structured illumination. Excitation light (488 nm, from an argon laser; Innova 90C; Coherent) was coupled via an acousto-optic deflector (AOM-40 AF; Intra-action) into a polarization-maintaining single-mode fiber (Oz Optics). The acousto-optic deflector was used as a fast shutter and intensity control. Light exiting the fiber was collimated and sent through a pattern generator (**Supplementary Fig. 2**) consisting of a 1,024 × 768 pixel ferroelectric liquid crystal on silicon SLM (Displaytech), a polarizing beam splitter cube and a half-wave plate. The light exiting the pattern generator was directed toward the microscope through a polarization rotator (**Supplementary Fig. 3**) consisting of two custom ferroelectric liquid crystal phase retarders with one-third–wave retardance (Displaytech) and a quarter-wave plate. Unwanted diffraction orders, caused by the finite-sized pixels of the SLM (**Supplementary Fig. 4**), were blocked by a mask located in a pupil plane. The desired ± 1 diffraction orders were refocused to points near opposite edges of the back focal plane of the microscope objective. After being recollimated by the objective lens (CFI Apo TIRF ×100, NA 1.49; Nikon), each beam approached the cover slip surface at an angle larger than the critical angle for total internal reflection. Evanescent waves from the two beams interfered to produce a line pattern of excitation intensity. Fluorescent emission light from the specimen was directed toward a camera by a dichroic mirror, as in a conventional fluorescence microscope. The dichroic mirror (403/488TPC-22.5deg; Chroma) used a custom coating with minimal transmission retardance at the excitation wavelength to maintain the desired polarization state, was deposited on an 3.2-mm-thick optically flat substrate to minimize aberrations in the reflected emission light and was operated at 22.5° to minimize aberrations in the transmitted excitation light.

The SLM was operated as a binary phase modulator, with each pixel producing a phase shift of nominally zero radians in its off state or π radians in its on state (that is, if written to with a binary 0 or 1, respectively).

To optimize the beam spacing in the pupil plane to match the TIRF zone diameter (**Supplementary Fig. 4**), the SLM projection lens (the lens located between the beam splitter cube and the polarization rotator in **Supplementary Fig. 1**) was implemented as a lens pair consisting of an achromat with a focal length of 350 mm and singlet with 7,500 mm focal length; the effective focal length of the combination could then be adjusted by changing the distance between the two lenses. The SLM pixel pitch, referred to sample space, was about 60 nm; the illumination pattern line spacing corresponded to 3 SLM pixels or ~0.18 μm. The 1,024 × 768 pixels of the SLM thus suffice for illuminating a field of ~61 × 46 μm, which is larger than the field of view of the camera: 512 × 512 pixels of size 63 nm, covering a field of 32 × 32 μm.

The ferroelectric liquid crystals were driven with a direct current electric field, with opposite directions for the on and off pixel states; this field must time-average to zero to avoid slow deterioration of the device through charge migration. Each pixel must thus spend equal time on and off. To this end, each pattern was polarity-switched (switching on pixels to off and vice versa) halfway through each raw exposure; both polarities produce the same illumination pattern in the sample. The illumination light was turned off by the acousto-optical shutter while a new pattern was being written to the SLM.

The illumination intensities quoted in the main text are the nominal ones: incident power divided by the field of view. The actual photon flux in the TIRF zone (given by the Poynting vector, which in the TIRF zone is parallel to the interface) varied rapidly with depth, reaching an estimated 4–6 times the nominal intensity immediately adjacent to the cover glass and decreasing exponentially with depth with a decay constant of ~100 nm.

System control. The desired patterns for one time point were preloaded onto the SLM controller peripheral component interconnect (PCI) circuit board. A digital signal processing PCI board (M67; Innovative Integration), running a program based on hardware-timed interrupts, generated transistor-transistor logic (TTL) signals at precisely controlled times to gate the acousto-optic shutter, trigger the camera to initiate frame transfer, switch polarity on the liquid crystal retarders in the polarization rotators, and trigger the SLM controller to load the next pattern onto the SLM.

Transfer function. An empirical point spread function was measured by imaging a 100-nm-diameter in-focus fluorescent microsphere (Yellow-Green Fluospheres; Invitrogen) dried onto a cover glass and mounted in water. An optical transfer function was calculated by 2D Fourier transforming the background-subtracted point spread function, dividing out the phase gradient corresponding to the bead position and rotationally averaging the result.

Acquisition. At each time point, raw SIM data were acquired at phases 0, 2π/3 and 4π/3 of the illumination pattern, for each of the three pattern orientations. The back-illuminated EMCCD camera (iXon DU-897 BI; Andor) was operated in frame transfer mode at −78 °C with water cooling (to avoid fan vibrations) and read out at 10 MHz with 14-bit digitization. The digital parameter that controls the electron multiplication gain (and which for this camera is nonlinearly related to the actual gain factor) was adjusted for each dataset depending on sample brightness, typically in the range 2,000–3,000.

Data processing. SIM data were reconstructed as described[2,20]. The process, done independently on each time point, is summarized below.

As a precaution against edge-related artifacts, the raw data were typically preprocessed by slightly intermixing opposing lateral

edges (the outermost ~10 pixels). Where not indicated otherwise, all raw data images in each time series were rescaled to equalize their total background-subtracted intensity, to compensate for light source intensity fluctuations and photobleaching. Because of its low signal and high background noise, the fastest kinesin dataset (**Supplementary Video 8**) was instead bleach-corrected based on curve-fitting to the whole sequence.

For each pattern orientation d, the three images taken at different illumination phases were each Fourier transformed spatially and then 'separated' (Fourier transformed with respect to the phase shift variable), resulting in three information components $D_{d,m}$ representing information that had been moved in frequency space, through mixing with the illumination pattern, by vectors $-m\mathbf{p}$, where $\mathbf{p}$ is the spatial frequency of the illumination pattern and $m = -1$, 0 and +1 for the three components.

For each pattern orientation d, precise values of the pattern wave vector $\mathbf{p}_d$, the starting phase and the modulation depth were determined from the data by comparing the $m = 1$ and $m = 0$ components in the region of frequency space where they overlap. To equalize the scaling so as to allow direct comparison, each component was first multiplied by a version of the optical transfer function that had been shifted to be centered at the position of the other component. The two components were then cross-correlated in three steps: first a standard fast Fourier transform–based cross-correlation in frequency space (yielding values only at discrete frequency-space pixels), then parabolic interpolation to locate the peak of that cross-correlation to subpixel accuracy and finally refinement through an optimization search in which subpixel frequency-space shifts were applied in the form of real-space phase gradients. The location of the cross-correlation peak yields the shift vector $\mathbf{p}_d$; the modulation depth a_d and starting phase φ_d were then found by complex linear regression on corresponding pixel values from the $m = 1$ and $m = 0$ components[20].

In the time series reconstructions presented here, these parameters were independently fit to the data for each time point. In practice, we have not observed any significant drift of the pattern parameters within any dataset. It would thus be possible to do global parameter fits on the entire dataset. Doing so would make the fit more robust against noise, and could improve the reconstruction quality drastically when the signal-to-noise ratio of the raw data is low. Some parameters, such as the pattern angles and line spacing, may in fact be stable enough that they can be assumed known without any fitting.

Once the parameters were determined, the different information components were combined through a generalized Wiener filter:

$$R(\mathbf{k}) = \frac{\sum_{d,m} O(\mathbf{k}+m\mathbf{p}_d)a_d e^{-i\varphi_d} D_{d,m}(\mathbf{k}+m\mathbf{p}_d)}{\sum_{d',m'} |O(\mathbf{k}+m'\mathbf{p}_{d'})a_{d'}|^2 + w^2} A(\mathbf{k}) \qquad (1)$$

where $R(\mathbf{k})$ is the value of the reconstruction (that is, the estimate of the true sample information $S(\mathbf{k})$) at the point $\mathbf{k}$ of frequency space, the sums were taken over the three pattern orientations and the three information components for each orientation, w^2 is the Wiener parameter (which was taken to be a constant and adjusted empirically), and $A(\mathbf{k})$ is an apodization function (typically a 2D triangle function, which decreases linearly from unity at the origin to zero at the extended resolution limit).

To avoid amplifying edge effects, equation (1) was implemented in the manner described in reference 20: each unshifted information component was separately multiplied by a filter function representing the other factors in its term of equation (1); the filtered results were then padded with zeros (to provide space for shifting information by the pattern vectors $\mathbf{p}_d$ or equivalently to decrease the real-space pixel size to accommodate the increased resolution), transformed to real space, multiplied by the complex phase gradient

$$e^{2\pi i m \mathbf{p}_d \cdot \mathbf{r}}$$

(which represents the frequency-space shift by the pattern wave vector $\mathbf{p}_d$), and added together, to produce the final reconstruction.

Image analysis and figure preparation. Image analysis and rendering was done with the Priism software package developed at the University of California, San Francisco. The final figures were assembled in Illustrator (Adobe).

Conventional images for comparison were synthesized from the SIM raw data by, at each time point, summing the raw data images for all orientations and phases. Doing this, as opposed to acquiring a separate conventional dataset, assures that the comparisons between conventional and SIM images are done for exactly equivalent conditions of excitation exposure and photobleaching.

The kymographs shown in **Figures 2c** and **3e** were produced by a horizontal maximum-intensity projection of the indicated areas for each time point. The 3D kymograph **Figure 3d** was produced by treating the *x*-*y*-time dataset as a 3D volume and making maximum-intensity projections through this volume along a viewing direction in *x*-*y*-time space. The 3D kymograph video in **Supplementary Videos 6** and **8** were produced by repeating the same process multiple times while successively rotating the viewing direction vector around the time axis.

The Fourier space images shown in **Figure 1d**,**e** and **Supplementary Video 2** were displayed using a nonlinear grayscale (gamma = ~0.4) and with the high values near the origin truncated to visualize clearly the weaker high-resolution information.

To decrease the file sizes of **Supplementary Videos 1**, **3**, **4** and **5**, the SIM reconstructions were binned 2 × 2, thus reducing them from 1,024 × 1,024 to 512 × 512 pixels, and the datasets were slightly cropped. Because the raw image data were somewhat oversampled as acquired (a pixel size of 63 nm, compared to the Nyquist limit of 84 nm based on the objective's numerical aperture and of about 120 nm based on its effective resolution), the pixelation of the binned videos is still sufficiently fine that the increased resolution can be appreciated. The data for **Supplementary Video 7** were similarly binned from 512 × 512 to 256 × 256 pixels. For **Supplementary Video 9**, which covers a smaller area, the conventional images were instead up-sampled to match the full-resolution SIM reconstruction. **Supplementary Video 2** was prepared by Fourier-transforming the full-resolution, full-field data and binning the result 2 × 2 in frequency space. The 3D kymograph in **Supplementary Video 6** was generated by first producing full-resolution projections through the full-resolution data volume and then binning the resulting video 2 × 2.

21. Rogers, S.L., Rogers, G.C., Sharp, D.J. & Vale, R.D. *J. Cell Biol.* **158**, 873–874 (2002).
22. Griffis, E.R., Stuurman, N. & Vale, R.D. *J. Cell Biol.* **177**, 1005–1015 (2007).
23. Maiato, H., Rieder, C.L. & Khodjakov, A. *J. Cell Biol.* **167**, 831–840 (2004).

doi:10.1038/nmeth.1324